View metadata, citation and similar papers at core.ac.uk

brought to you by CORE

provided by E-space: Manchester Metropolitan University's Research Repository

Fornaciari, Julie C and Gerhardt, Michael R and Zhou, Jie and Regmi, Yagya N and Danilovic, Nemanja and Bell, Alexis T and Weber, Adam Zev (2020) The Role of Water in Vapor-fed Proton-Exchange-Membrane Electrolysis. Journal of the Electrochemical Society. ISSN 0013-4651

**Downloaded from:** http://e-space.mmu.ac.uk/625966/

**Version:** Accepted Version

**Publisher:** The Electrochemical Society

**DOI:** https://doi.org/10.1149/1945-7111/ab9b09

**Usage rights:** Creative Commons: Attribution 4.0

Please cite the published version

https://e-space.mmu.ac.uk

# The Role of Water in Vapor-fed Proton Exchange Membrane Electrolysis

Julie C. Fornaciari[1, 2], Michael R. Gerhardt, [1] Jie Zhou[1], Yagya N. Regmi[1], Nemanja Danilovic[1], Alexis T. Bell[2, 3], Adam Z. Weber[1]

[1] Energy Storage and Distributed Resources Division, Lawrence Berkeley National Laboratory, Berkeley, CA 94720
[2] Department of Chemical and Biomolecular Engineering, University of California Berkeley, Berkeley CA 94720
[3] Joint Center for Artificial Photosynthesis, Lawrence Berkeley National Laboratory, Berkeley, CA 94720

Water-vapor fed electrolysis, a simplified single-phase electrolyzer using a proton exchange membrane electrode assembly, achieved >100 mA/cm$^2$ performance at <1.7 V, the best for water-vapor electrolysis to date, and was tested under various operating conditions (temperature and inlet relative humidity (RH)).To further probe the limitations of the electrolyzer, a mathematical model was used to identify the overpotentials, local water activity, water content values, and temperature within the cell at these various conditions. The major limitations within the water-vapor electrolyzer are caused by a decreased water content within the membrane phase, indicated by increased Ohmic and mass transport losses seen in applied voltage breakdowns. Further investigations show the water content (λ, mole of water/mole of sulfonic acid) can decrease from 13 at low current densities down to 6 at high current densities. Increasing the temperature or decreasing RH exacerbates this dry-out effect. Using our mathematical model, we show how these mass transport limitations can be alleviated by considering the role of water as both a reactant and a hydrating agent. We show that low cathode RH can be tolerated as long as the anode RH remains high, showing equivalent performance as symmetric RH feeds.

# Introduction

Hydrogen is garnering increasing attention for multiple applications, such as transportation and long-term storage of electrical energy[1-5]. Green hydrogen is produced from renewable electricity via water electrolysis, where the half-reactions are the oxygen-evolution reaction (OER) and hydrogen-evolution reaction (HER)

$$2H_2O \rightarrow O_2 + 4H^+ + 4e^- \qquad U = 1.23\,V\ vs\ SHE, \tag{1}$$

$$4H^+ + 4e^- \rightarrow 2H_2 \qquad U = 0.00\,V\ vs\ SHE. \tag{2}$$

at the anode and cathode at standard conditions and in an acid environment, respectively. Recent studies have shown that high current densities (up to 1-5 A/cm$^2$) can be achieved using a membrane-electrode assembly (MEA), shown in Figure 1.[6-8] The MEA comprises a solid-state electrolyte, typically a proton-exchange membrane (PEM), catalyst layers, and diffusion or transport media. Each component assists in transporting the reactants/products to/from the reaction sites as well as transporting ions and electrons to complete the electrochemical reactions.[7] The MEA architecture, which originated from polymer-electrolyte fuel cells, optimizes mass and ohmic transport through its various porous layers and enables use of high surface area catalysts within the porous catalyst layers, while concomitantly minimizing cell ohmic losses through the use of thin, conductive polymer membranes.[8-10] Thus, it is a preferred design for use in vapor electrolysis.

Conventional electrolyzers utilize liquid water, which needs to be ultra-pure because contaminants can poison and degrade the electrocatalysts and the membrane.[11,12] Moreover, liquid-fed electrolyzers exhibit a high electro-osmotic flow of water from anode to cathode, which results in a saturated hydrogen stream that must be dried before compression and storage.[7] Furthermore, the use of this architecture for more complex reactions (e.g., carbon dioxide or nitrogen reduction)

encounters problems due to the low solubility of the gaseous reactants. [13,14] Another issue is that bubble formation in liquid feeds can introduce transport problems and light scattering when the MEA architecture is used for photo-electrochemical water splitting.[15-17] The above issues can be ameliorated by using a water-vapor instead of a liquid-water feed.

Vapor-fed electrolysis significantly simplifies the physics and operation of MEA cells. It also provides the opportunity to use non-conventional water inputs, such as seawater-vapor,[18,19] and opens up the possibility of electrolysis in semiarid regions or locations where clean liquid water is not readily accessible.[20] Compared to liquid feeds, operating with water vapor is expected to result in significant mass-transport and nonlinear Ohmic limitations, with the latter stemming from decreased membrane and ionomer hydration with water vapor due to the dependence of ionic conductivity on hydration for traditionally used proton-exchange membranes like Nafion.[21,22] There have been limited investigations of water-vapor fed electrolysis. The systems reported to date exhibit stable performance but low current densities (<100 $mA/cm^2$).[15,17,19,23] Therefore, there is a need for detailed exploration of the possibilities and limitations of this operating paradigm, especially as it concerns the interplay of water consumption, diffusion, and electro-osmosis within an MEA system.

In this paper, we explore vapor-fed electrolysis with a focus on cell operating conditions and the role of water within the MEA. Our objective is to explore the causes of high overpotentials within the cell. Detailed understanding of global and local effects is accomplished through combined experimental and theoretical investigations of the underlying phenomena. First, the experimental and modeling methodologies are introduced. Next, the measured performance of a vapor-fed electrolyzer operated at room and elevated temperature is demonstrated and discussed. Then a model is used to dissect the results using an applied voltage breakdown in order to describe

the impact of relative humidity and potential losses in different parts of the cell. Finally, the role of water vapor supply is investigated by examining the effects of supplying the anode and cathode compartments with feeds differing in relative humidity.

# Experimental

## Membrane-Electrode-Assembly Fabrication

The MEA (Figure 1) comprises a catalyst-coated membrane (CCM). The two catalyst layers (CLs) were formed by spray coating the respective sides of a Nafion 117 membrane (Ion Power, Delaware, USA) using a Sono-Tek ultrasonic spray coater (Sono-Tek Exacta Coat, New York, USA). For all tests, the Nafion membrane was pre-soaked in 95°C water for one hour and pre-treated in room temperature 0.5 M nitric acid bath for one hour to remove any impurities. The membranes were stored in deionized water before the spray coating of catalyst layers, which were dried while on the heated vacuum plate of the spray coater. The MEA is sandwiched between a 255-μm thick titanium porous transport layer (PTL) (Proton OnSite, Connecticut, USA) on the anode CL and a 190 μm-thick carbon gas-diffusion layer (GDL) covered by a 45 μm-thick microporous layer (MPL) (Sigracet 29BC, SGL Wiesbaden, Germany) on the cathode CL. Gas is supplied to both the PTL and the GDL using two graphite single serpentine flow channels (Fuel Cell Technologies Inc., 1 mm thick land and channel). Although graphite is not thermodynamically stable at the anode potentials used in this study,[24] none of the tests in this paper were held for longer than 2 h. No degradation of the graphite flow-fields was observed in the 2 h tests, as there was no $CO_2$ formed at 500 mA/cm$^2$ for 16 h when the outlet of the cell was monitoring gas evolution with a real time gas analyzer mass spectrometer (Diablo Analytical, California, USA). To minimize contact resistance, the carbon GDL is compressed to 20% and to assure no gas leaks throughout the cell, PTFE (McMaster-Carr), or Tefzel™ gaskets (CS Hyde, Illinois, USA) of 0.18-

mm and 0.254-mm thickness, were used on the cathode and anode sides of the assembly, respectively.

The catalyst inks were composed of catalyst nanoparticles, iridium black for the anode and 45.9 wt.% platinum on Vulcan carbon for the cathode (both from TKK, Tokyo Japan), Nafion ionomer (Ion Power, Delaware), water, n-propanol, ethanol mixtures for the iridium ink and n-propanol and water mixture for the platinum ink (exact recipes are given in Table S1). These inks were spray-coated directly onto the Nafion 117 membrane using a 120 kHz nozzle. The target loadings were ~1 mg/cm$^2$ Ir on the anode and ~0.3 mg/cm$^2$ Pt on the cathode. A relatively high platinum loading was used for the cathode to ensure that the cell was not limited by the hydrogen-evolution reaction. The total active area (geometric) was 5 cm$^2$ for each electrode.

## Test Protocol

Electrochemical tests were performed using a commercial test stand (Fuel Cell Technologies Inc. (FCT), New Mexico, USA). Ultra-high purity argon (99.999%) was bubbled through a temperature-controlled bubbler with 18.2 MΩ deionized water (EMD Millipore, Billerica MA). The gas flow rates, cell temperature, and bubbler temperature were controlled independently to achieve a cell relative humidity (RH) of 30 to 98%. All tests were at ambient pressure and either 30°C or 80°C. The flowrate of gas to each side of the cell was 200 mL/min. For liquid-fed electrolysis, liquid water was introduced into the anode compartment using an external diaphragm pump (KNF NF25) at a flow rate of 100 mL/min. Electrochemical testing was performed using a Biologic VSP-300 potentiostat with 5 A booster (Seyssinet-Pariset, France). Electrochemical impedance was measured in potentiostatic mode, by imposing a 10 mV perturbation between 200 kHz – 100 mHz at several cell voltages in order to generate a Nyquist plot, where the intercept with the real axis is the measured high frequency resistance (HFR) of the cell.

Each MEA was conditioned by flowing humidified argon (98% RH) to both sides of the cell for at least one hour at open circuit voltage. Chronopotentiometric steps were then applied, starting from 10 mA/cm$^2$ and increasing to 1000 mA/cm$^2$, or until the MEA reached the cutoff potential 2.3 V, chosen to prevent corrosion of cell flow fields, endplates, and current collectors. A step size of 10 mA/cm$^2$ was used at low current densities, and 50 mA/cm$^2$ was used for higher current densities. Each current density step was 2 min or until a stable response was reached (± 50-100 mV), and the voltage response data were averaged over the last 20 s for the polarization curve. Two polarization curves were collected for each MEA, with multiple MEAs tested for each set of electrolyzer test conditions.

## Mathematical Model

A mathematical model of vapor-fed electrolysis in an MEA was used to interpret the experimental data. A 2-D view of the model domain is shown in Figure 1 and Figure S1. The governing differential equations and their boundary conditions are given in Tables S2-S5 of the supporting information. The characteristic properties for each domain (materials properties, dimensions, etc.) are detailed in Tables S6-S10.

This model was adapted from fuel-cell models developed by Balliet et. al.[25] and Zenyuk, Das, Weber.[26] Mass transport within each component domain is governed by the same mass transport mechanisms as those considered for the modeling of fuel cells, namely multicomponent diffusion and convection via Darcy's law for the porous media and concentrated-solution theory for the membrane and ionomer. In contrast to the fuel-cell models, the model is single phase and thus assumes no liquid water in the cell, which is justified due to an RH less than 100%, heat being generated, and water being consumed as a reactant. If water does condense, its influence is expected to be minimal although this could be a topic for future investigation and model

refinement. Additionally, the fuel cell model's reactions are changed to OER and HER (eq (1) and (2)) occurring at the anode and cathode, respectively. These two changes impact water movement within the system, as water is consumed at the anode in an electrolyzer, thereby limiting the flux of water to the anode side of the membrane. Water flux can still occur from the cathode side of the membrane to the anode depending on the balance between back transport and electro-osmosis in the membrane. Additionally, the model is non-isothermal and the effects of heat generation within the MEA are taken into account with an overall energy balance and appropriate boundary conditions (see Table S2 eq 10, Table S3, and Table S5). Heat generation and consumption occurs through ohmic heating, vaporization of water, and heat released in the reactions. In the vapor-fed system, one expects more severe temperature nonuniformities and local dehydration due to the increases temperature in the MEA, whereas in liquid-fed cell, the water acts as a coolant and temperature excursions are minimal.

The model was used to calculate various properties and characteristics of the MEA that are not accessible by experiments. An important characteristic is the net water flux through the membrane,

$$\boldsymbol{N}_{H_2O,PEM} = \frac{\xi \boldsymbol{i}}{F} - \alpha \boldsymbol{\nabla \mu_{H_2O}}, \tag{3}$$

where $\xi$ is the electro-osmotic coefficient, **i** is the current density, F is Faraday's constant, $\alpha$ is the diffusion coefficient, and $\mu_{H_2O}$ is the chemical potential of water within the membrane. The first term on the right side of this equation represents water transport by electro-osmosis and the second term represents water transport by diffusion.

The model is also used to determine the water content, temperature distribution and the contribution to the applied voltage within the MEA cell. Using the methodology of Gerhardt et. al.[27] the applied-voltage breakdown (AVB) is given by

$$V = U^{ref} + \eta_{HER,BV} + \eta_{OER,Tafel} + \eta_{MT} + \eta_{cathode,ionomer} + \eta_{anode,ionomer} + \eta_{PEM,} \quad (4)$$

where $U^{ref}$ is the Nernstian thermodynamic potential (referenced to the conditions in the gas channel), $\eta_{HER,BV}$ and $\eta_{OER,Tafel}$ are the kinetic overpotentials for the cathode and anode reaction, respectively, $\eta_{i,ionomer}$ is the Ohmic loss from the ionomer within the CL, $\eta_{MT}$ is the mass-transport losses within the anode CL, and $\eta_{PEM}$ is the Ohmic loss across the membrane. The dependence of these terms on current and properties of different parts of the MEA are given in Table S11. The cathode CL has negligible mass-transport losses as the reactant protons are at fixed concentration set by the reaction rate and any transport losses are Ohmic in nature. The electronic losses are minimal due to the high conductivity of the electronically-conducting materials.

## Theory: Role of Water

Before examining the data, it is important to identify the different types of water flux occurring in the system and their impact on the maximum possible performance of the MEA. In electrolysis, water is not only a reactant, but also a hydrating agent. Furthermore, water transport through the system is complex due to the various driving forces (see, for example, eq. (3)). At steady state, a water mass balance at the anode catalyst layer results in

$$\mathbf{N}_{H_2O,PTL} - \mathbf{N}_{H_2O,PEM} = \frac{\mathbf{i}}{2F}, \quad (5)$$

where $N_{H_2O,PTL}$ is the water flux through the PTL from the water-vapor feed stream and $\mathbf{N}_{H_2O,PEM}$ is the net water flux through the membrane. The extent to which water leaves or comes through the membrane can be described by the net electro-osmotic coefficient, β,[27,28]

$$\beta = \frac{\mathbf{N}_{H_2O,PEM}\, F}{\mathbf{i}}. \quad (6)$$

A positive value of β means that the net water movement is from anode to cathode and a negative value of β corresponds to water moving from cathode to anode. With no net water flux in the membrane (i.e., $N_{H_2O,PEM} = 0$, β=0), a current density can be defined as

$$i_{\beta=0} = 2FN_{H_2O,PTL} = 2F\frac{(C_o - 0)D^{eff}}{t_{PTL}} \quad (7)$$

where $c_o$ is the concentration in the gas channel, $D^{eff}$ is the effectivity diffusivity of water within the gas phase of the porous media in the anode, and $t_{PTL}$ is the thickness of the PTL. $i_{\beta=0}$ is a function of temperature, as shown in Figure 2b (at 98% RH), because both $D^{eff}$ and $c_o$ are functions of temperature. Eq. (7) is written assuming limiting current and a linear gradient from the channel to the reaction site. Combining eqs. (5)-(7) and normalizing by $i_{\beta=0}$ we obtain an expression for the nondimensionalized maximum current density

$$\frac{i_{max}}{i_{\beta=0}} = \frac{1}{(1+2\beta)}, \quad (8)$$

Figure 2a plots eq. (8). Eq. 8 can also be written as a function of chemical potential as shown in the SI. The critical impact of water flux through the membrane is evident by its influence on the maximum achievable current density. Since the electro-osmotic flux of water through the membrane influences how much water is available to react in the anode catalyst layer, the maximum current density is a function of current, which dictates the magnitude of the electro-osmotic flux. For example, $i_{max}$ goes from 1.22 A/cm$^2$ for 98% RH feed at 30°C for β = 0 to ~400 mA/cm$^2$ for β = 1, corresponding to pure electro-osmotic flow. The reason for this trend is that an increase in β results in a reduction in the availability of water for reaction. Conversely, if there is net water transport from the cathode (e.g., due to different membrane design or operating conditions), a higher than expected maximum current is possible. It should be noted that for anode and cathode feeds with identical RH, β is typically slightly negative and sufficiently large in

magnitude to make simple analysis of electrolyzers complicated; thus, care is needed in analyzing the experimental data. Overall, Figure 2 provides a metric for experimentalists to determine how close to mass-transport-limiting conditions their system operates, since the water balance and the value of β are accessible experimentally. The water balance can be determined by measuring the inlet and outlet RH of both streams and accounting for the consumption of water by reaction.

# Results and Discussion

## Vapor-fed Electrolyzer Performance

Figure 3a compares the polarization curve for liquid- and vapor-fed electrolysis at 30°C. The liquid-fed MEA requires a lower voltage for a given current density. The voltage versus current-density curves are similar up to about 100 mA/cm$^2$. Above this current density, the voltage for the vapor-fed cell rises substantially relative to that for the liquid-fed cell and grows rapidly with increasing current density. This divergence between the vapor- and liquid-fed cases is mainly due to a loss of ion conductivity within the membrane brought about by inadequate membrane hydration (which includes RH changes due to water mass transport from the channel to the membrane surface) for the case of vapor-fed electrolysis. This finding is in agreement with the calculated HFR from our EIS data and the subsequent iR-corrected voltage vs current density plots in Figure S2 of the SI. We note that the iR-corrected plots are essentially the same for the vapor-fed and liquid-fed cases, indicating the supply of water does not limit the rate of reaction, which is consistent with the current being lower than $i_{max}$ as calculated via Equation 8 (see Figure 2). We also note that changing the flow field or increasing the inlet flowrate did not improve the performance as shown in Figure S3 and S4 in the SI.

Temperature has a significant impact on performance of the vapor-fed electrolyzer; not only does the maximum current density at 98% RH increase (see Figure 2b), but so do the kinetics

and the transport properties of the membrane and the ionomer. Figure 3b compares the polarization curves for liquid-fed electrolysis with vapor-fed electrolysis at 80°C. Increasing the temperature, decreases the voltage required for a given current density for both liquid and vapor cells. For example, the voltage required for a current density of 1000 $mA/cm^2$ is 1.92 V at 30°C, but decreases to 1.76 V at 80°C for the liquid-fed system. The same is true for the vapor-fed MEA, but in this case, the voltage difference for required for a current density of 320 $mA/cm^2$ at 30°C (2.3 V) and 80°C (1.67 V) is greater.

To identify the reasons for the large voltage required by the vapor-fed system, the total cell voltage versus current density and the AVB were calculated using the model of the 80°C vapor-fed MEA. Figure 4a shows that the model accurately describes the overall cell voltage versus current density measured experimentally. Figure 4b illustrates the AVB at 80°C. The largest voltage losses are associated with the OER kinetics, the Ohmic resistance of the membrane, and the mass-transport loss through the anode CL. The potential loss due to the OER kinetics is a characteristic of the iridium catalyst. As expected, the OER overpotential is larger than that for the HER, reflecting the slower kinetics of OER.[7] The Ohmic loss in the membrane increases rapidly with current density, and is a function of water activity within the membrane phase (as shown in Table S10). The mass-transport loss within the anode CL (see eq. 16 in Table S11) corresponds to the influence of changes in the reactant water concentration between the gas pathways, reaction sites, and ionomer. The origin of these mass-transport losses is caused by a combination of CL underutilization (discussed in further detail below), and local temperature rise.

The effects of current density on the distribution of water in the electrolysis cell is shown in Figure 4c. As the current density increases, the local cell temperature increases (see Figure S5), which exacerbates the mass-transport-related decrease in RH at the CL; the membrane water

content ($\lambda$) or moles of water per sulfonic acid site, is similarly depressed. For 150 mA/cm$^2$, $\lambda$ is about 13, whereas for 680 mA/cm$^2$ the value of $\lambda$ is about 6. For reference, a maximum value of $\lambda$=16 for fully hydrated Nafion has been observed previously.[21,29,30] Thus, at the operating current densities at which the vapor electrolyzer is running, the value of $\lambda$ is far from the saturated value.

To explore the effects of overall water transport in more detail, the carrier gas was changed from argon to helium in order to decrease any bulk transport effects in the PTL since the water-vapor diffusivity through helium is three times larger than that through argon. As shown in Figure 5a, going from argon to helium results in a monotonic, nonlinear decrease in the overall cell voltage with current density. Although the gradient within the PTL is small, the higher diffusivity provides better water transport to the reaction sites, which leads to a higher local RH on both sides of the membrane at a given current density. The higher local RH leads to higher water content within the membrane phase (Figure 5a, right axis), demonstrating that helium results in better hydration. Since the membrane is better hydrated, secondary effects, such as water transport from the cathode to the anode and maximum cell temperature, further assist in mitigating overpotential losses. The maximum cell temperature when argon and helium are used is 91.4°C and 89.9°C, respectively, which is enough to reduce the overpotential by 150 mV. The reduction in overpotential is primarily Ohmic, with only a secondary effect on kinetics due to higher reactant concentration.

Figure 5b shows that decreasing the membrane thickness (from 183 to 25 μm) has a substantial impact on performance. The thinner membrane exhibits a lower Ohmic loss because it promotes back transport of water in the membrane and thus a more negative value of $\beta$ (see eqs. 6 and 8 and Figure 2), which helps to keep the membrane better hydrated,[31,32] in addition to simply being thinner. However, the decrease in membrane thickness is known to increase product gas crossover and thus lower cell efficiency.[7,33,34] Such effects become compounded by the fact that

most electrolyzers operate with pressure differentials as higher pressure hydrogen is desired.[33] The tradeoffs between electrolyzer performance, gas crossover, and optimal operating pressure must be considered by system designers and is an active area of research.

## Effects of difference in the RH of the anode and cathode feeds

Many of the proposed applications for vapor-fed electrolyzers are expected to have inlet streams that are not fully humidified or involve a water-vapor-feed to only one electrode. Different humidity levels in the anode and cathode feeds can help prevent excess water reaching the cathode, where wet hydrogen is difficult to store and use, as discussed earlier. To explore these effects and further comprehend the role of water on cell performance, the feed RH was varied, as shown in Figure 6. As expected, the cell voltage increases with reduced feed RH. Nevertheless, even at 30% RH and 80°C, a current density of 160 mA/cm$^2$ is achieved at 2.08 V, comparable to the low-temperature study shown in Figure 3a. Interestingly, the inlet water-vapor concentrations are comparable for a feed with a 30% RH at 80°C (0.0049 mol/L) and a feed with a 98% RH at 30°C (0.0017 mol/L). Nevertheless, the measured voltage is not the same above 50 mA/cm$^2$. As shown in Figure S6, a feed with 30% RH at 80°C requires higher voltage for a given current density. This observation demonstrates that cell voltage is more dependent on water activity than water concentration: at 80°C, the activity is 0.30 ($\lambda = 4.47$), but at 30°C, the activity is 0.98 ($\lambda = 14.94$). This agrees as well with our modeling assumption and hypothesis that activity drives the reaction.

AVBs obtained from the model of the vapor-fed electrolysis cell operated at 150 mA/cm$^2$ are shown in Figure 7 as a function of the RH of the feed at 80$^o$C. Figure 7a shows the absolute values of each component of the overpotential and Figure 7b shows the relative contributions of each component. The impact of anode mass transport and Ohmic losses are evident at 30% RH where the mass transport accounts for 31% and the Ohmic loss accounts 28% of the total overpotential, Interestingly, at 98% RH, the mass-transport losses are still high, accounting for

43% of the total overpotential, but the Ohmic overpotential only makes up only 7% of the total overpotential loss. This result further highlights the importance of water activity within the membrane phase on the overall cell performance. At lower RHs, the low level of membrane and ionomer hydration significantly impacts conductivity of these phases, resulting in increased Ohmic loss within both components.

The CL is a heterogeneous, multicomponent structure that requires percolation pathways for water, ions, and electrons to reach the embedded catalyst sites. Due to this complexity and the interrelation of phenomena in the CL, unambiguous deconvolution of the mass-transport overpotentials is difficult, especially as the properties of all components depend on the state of their hydration.[21,35] As shown in Figure 8a, the reaction-rate distribution within the anode CL shifts from being uniform throughout the catalyst layer at 98% RH, to being steep near the membrane:anode CL boundary at 30% RH. Such a change is indicative of going from conditions where the rate of the OER is kinetically limited to one where this reaction is limited by ionic transport. In the latter case, the reduced water activity limits the availability of water, resulting in a lower water content in the membrane, as shown in Figure 8b. Another consequence of the reduction in ionomer hydration with decreasing feed RH is that the total overpotential loss in the anode CL increase in order to maintain constant current density.[35] This effect is shown in Figure 8c.

Water moves through the cell in different phases and with different driving forces, as discussed above. To explore the effects of water transport further, experiments were conducted with unequal ("asymmetric") humidities in the anode and cathode feeds. The results of these experiments are shown in Figure 9a. Comparison of cell polarization curves reveals that water supply to the anode is more important than water supply to the cathode, because at 2 V, the current

density is markedly higher when the anode feed is higher RH. Also shown in Figure 9a is the "symmetric" case, in which the RH of each feed is set to the average RH of the asymmetric RH experiment. This experiment affirms that at low current densities the kinetic losses dominate (i.e., the symmetric RH curve is aligned with that for the drier anode asymmetric curve, as shown in the inset), while at higher current densities mass transport and Ohmic effects dominate (i.e., the symmetric RH curve aligns closer to the drier cathode asymmetric curve). These trends agree with the AVBs presented in Figure 7.

Insights into the mechanism of water-transport and its effects on overall cell polarization were obtained by calculating the value of β, the net water flux through the membrane normalized by the proton flux (see eq. (6)), i.e., a net electro-osmotic coefficient. The results for three cases are presented in Figure 9b. This calculation was done using the model of the vapor-fed electrolyzer. For the cases in which asymmetric RH is used in the anode and in the cathode feed, back transport via diffusion dominates the response, regardless of the direction of the electro-osmotic flow. At lower current densities, the lower RH anode case benefits from this transport, as β helps move water to the anode and the cell has similar performance as the symmetric RH case. However, at higher current densities, electro-osmosis drives β to be more positive and move water away from the anode reacting site. Even though β continues to be negative for the low RH anode case, this experiment shows that lower local RH at the anode CL can reduce the achievable current density at 2.0 V, emphasizing the importance of anode RH on performance. The experiments also demonstrate that there is little benefit of feeding the anode and the cathode with the same RH. A high RH in the feed to the anode is sufficient to provide water to the cathode and can sustain reasonable current densities.

# Summary

We have shown that a vapor-fed MEA system for the electrolysis water can be operated at current densities above 100 mA/cm$^2$. In contrast to liquid-fed electrolyzers, in which water supply is not an issue, the water content of the vapor-fed plays a significant role as both a hydrating agent and a reactant. This dependence on water content is especially true under conditions where the maximum achievable current densities are compromised due to electro-osmotic flows in the system that further decrease water activity at the reaction site. Analysis of the vapor-fed electrolyzer, using a mathematical model, demonstrates conclusively that the most important role of water is in hydrating the ionomer in the catalyst layers and the membrane, with higher humidity and temperatures leading to higher current densities for a given applied voltage. The computed reaction distribution with the anode catalyst layer suggests underutilization of this catalyst layer (where the OER occurs), especially at low anode feed humidities. We have also demonstrated that a high relative humidity in the anode feed is critical for good electrolyzer performance. Our study illustrates how feed composition and operating conditions affect the performance of a vapor-fed electrolyzer, information that will be useful for the design of vapor-fed electrolyzers for practical applications.

# Acknowledgements

The authors acknowledge Shell's New Energies Research and Technology (NERT) and the Energy & Biosciences Institute through the EBI-Shell Program, as well as the HydroGen Energy Materials Network from the Fuel Cell Technologies Office of DOE for partial funding on this project. JCF thanks the National Science Foundation (grant DGE 1106400) for support. The authors thank Shell NERT's Methane to Products (M2P) program, Dr. Xiong Peng, Dr. Darinka Primc, Anamika

Chowdhury, Zachary Taie, Ashley Werre, and Sarah Berlinger for insight and discussions; Proton OnSite/NEL Hydrogen for Ti PTLs. JCF, YNR, ND, ATB, and AZW designed and conducted experiments. JCF, MRG, and JZ modified and ran COMSOL simulations. JCF, MRG, ATB, and AZW composed the manuscript, and all authors edited the written work.

# Nomenclature

| | |
|---|---|
| Abbreviations | |
| AVB | Applied voltage breakdown |
| BV | Butler-Volmer Kinetics |
| CCM | Catalyst-coated membrane |
| CL (aCL or cCL) | Catalyst layer (anode or cathode) |
| FCT | Fuel cell technologies |
| GDL | Gas diffusion layer |
| HER | Hydrogen evolution reaction |
| MEA | Membrane electrode assembly |
| MPL | Microporous layer |
| MT | Mass transport |
| OER | Oxygen evolution reaction |
| PEM | Proton exchange membrane |
| PTL | Porous transport layer |
| RH | Relative humidity |
| SHE | Standard hydrogen electrode, 0.0 V |
| | |
| Roman | |
| $C_o$ | Initial concentration, mol/m$^3$ |
| $D^{eff}$ | Effective diffusivity, m$^2$/s |
| $F$ | Faraday's Constant (96485 C/mol) |
| $i$ | Current density, mA/cm$^2$ |
| $i_{max}^{D}$ | Diffusional maximum current density, A/cm$^2$ |
| $i_{max}$ | Maximum current density, A/cm$^2$ |
| $\mathbf{N}_{H_2O,PEM}$ | Molar water flux in the membrane, mol/cm$^2$s |
| $t_{PTL}$ | Thickness of the porous transport layer, m |
| $U^{ref}$ | Nernstian thermodynamic potential, V |
| $V$ | Applied Voltage, V |
| Greek | |
| $\alpha$ | Diffusion coefficient, mol$^2$/J cm s |
| $\beta$ | Normalized water flux within the membrane |
| $\eta_i$ | Overpotential in a domain i, V |
| $\lambda$ | Membrane water content, mol $H_2O$/mol $SO_3^-$ |
| $\mu_{H_2O}$ | Water electrochemical potential |
| $\xi$ | Electro-osmotic coefficient |

# References


1. K. Mazloomi and C. Gomes, Hydrogen as an energy carrier: Prospects and challenges, in *Renewable and Sustainable Energy Reviews*, p. 3024 (2012).
2. F. Barbir, PEM electrolysis for production of hydrogen from renewable energy sources, in *Solar Energy*, p. 661 (2005).
3. A. Buttler and H. Spliethoff, Current status of water electrolysis for energy storage, grid balancing and sector coupling via power-to-gas and power-to-liquids: A review, in *Renewable and Sustainable Energy Reviews*, p. 2440, Elsevier Ltd (2018).
4. J. D. Holladay, J. Hu, D. L. King and Y. Wang, An overview of hydrogen production technologies, in *Catalysis Today*, p. 244 (2009).
5. M. R. Shaner, H. A. Atwater, N. S. Lewis and E. W. Mcfarland, A comparative technoeconomic analysis of renewable hydrogen production using solar energy, in *Energy Environ. Sci*, p. 2354 (2016).
6. S. Shiva Kumar and V. Himabindu, Hydrogen production by PEM water electrolysis – A review, in *Materials Science for Energy Technologies*, p. 442, Elsevier BV (2019).
7. M. Carmo, D. L. Fritz, J. Mergel and D. Stolten, *International Journal of Hydrogen Energy*, **38**, 4901 (2013).
8. W. Dai, H. Wang, X. Z. Yuan, J. J. Martin, D. Yang, J. Qiao and J. Ma, A review on water balance in the membrane electrode assembly of proton exchange membrane fuel cells, in *International Journal of Hydrogen Energy*, p. 9461 (2009).
9. E. H. Majlan, D. Rohendi, W. R. W. Daud, T. Husaini and M. A. Haque, Electrode for proton exchange membrane fuel cells: A review, in *Renewable and Sustainable Energy Reviews*, p. 117, Elsevier Ltd (2018).
10. L. M. Pant, Z. Yang, M. L. Perry and A. Z. Weber, JES FOCUS ISSUE ON PROTON EXCHANGE MEMBRANE FUEL CELL (PEMFC) DURABILITY Development of a Simple and Rapid Diagnostic Method for Polymer-Electrolyte Fuel Cells, in *Journal of The Electrochemical Society*, p. 3007 (2018).
11. S. Stucki, G. G. Scherer, S. Schlagowski and E. Fischer, in.
12. F. Andolfatto, R. Durand, A. Michas, P. Millet and P. Stevens, *International Journal of Hydrogen Energy*, **19**, 421 (1994).
13. D. Higgins, C. Hahn, C. Xiang, T. F. Jaramillo and A. Z. Weber, (2018).
14. Z. W. Seh, J. Kibsgaard, C. F. Dickens, I. Chorkendorff, J. K. Nørskov and T. F. Jaramillo, *Science*, **355** (2017).
15. J. M. Spurgeon and N. S. Lewis, *Energy & Environmental Science*, **4**, 2993 (2011).
16. T. A. Kistler, D. Larson, K. Walczak, P. Agbo, I. D. Sharp, A. Z. Weber and N. Danilovic, *Journal of The Electrochemical Society*, **166**, H3020 (2018).
17. P. K. Giesbrecht, a. M. Astrid M, c. G. Carlos Read, S. Holdcroft, N. S. Lewis and M. S. Freund, (2019).
18. r. Dresp, F. Dionigi, M. Klingenhof and P. Strasser, **15**, 31 (2020).
19. S. Kumari, R. T. White, B. Kumar and J. M. Spurgeon, *Energy Environ. Sci*, **9**, 1725 (2016).
20. S. Haussener, C. Xiang, J. M. Spurgeon, S. Ardo, N. S. Lewis and A. Z. Weber.
21. A. Kusoglu and A. Z. Weber, *Chem Rev*, **117**, 987 (2017).

22. H. Ito, T. Maeda, A. Nakano and H. Takenaka, Properties of Nafion membranes under PEM water electrolysis conditions, in *International Journal of Hydrogen Energy*, p. 10527 (2011).
23. G. Heremans, C. Trompoukis, N. Daems, T. Bosserez, I. F. J. Vankelecom, J. A. Martens, J. Rongé and R. Rongé, **7**, 50 (2017).
24. M. Pourbaix, *Atlas of Electrochemical Equilibria in Aqueous Solutions*, National Association of Corrosion Engineers (1966).
25. R. J. Balliet and J. Newman, *Journal of The Electrochemical Society*, **158**, B927 (2011).
26. I. V. Zenyuk, P. K. Das and A. Z. Weber, *Journal of The Electrochemical Society*, **163**, 691 (2016).
27. M. R. Gerhardt, L. M. Pant and A. Z. Weber, *Journal of The Electrochemical Society*, **166**, 3180 (2019).
28. A. Z. Weber, R. L. Borup, R. M. Darling, P. K. Das, T. J. Dursch, W. Gu, D. Harvey, A. Kusoglu, S. Litster, M. M. Mench, R. Mukundan, J. P. Owejan, J. G. Pharoah, M. Secanell and I. V. Zenyuk, *Journal of The Electrochemical Society*, **161**, 1254 (2014).
29. K. D. Kreuer, The role of internal pressure for the hydration and transport properties of ionomers and polyelectrolytes, in *Solid State Ionics*, p. 93, Elsevier B.V. (2013).
30. T. A. Zawodzinski, T. E. Springer, F. Uribe and S. Gottesfeld, Characterization of polymer electrolytes for fuel cell applications, in *Solid State Ionics*, p. 199 (1993).
31. A. Z. Weber and J. Newman, Transport in Polymer-Electrolyte Membranes III. Model Validation in a Simple Fuel-Cell Model, in (2004).
32. A. Z. Weber, Gas-Crossover and Membrane-Pinhole Effects in Polymer-Electrolyte Fuel Cells, in *Journal of The Electrochemical Society*, p. 521 (2008).
33. M. Schalenbach, M. Carmo, D. L. Fritz, J. Rgen Mergel and D. Stolten, (2013).
34. M. Schalenbach, T. Hoefner, P. Paciok, M. Carmo, W. Lueke and D. Stolten, (2015).
35. J. Newman and K. E. Thomas-Alyea, *Electrochemical systems*, John Wiley & Sons (2012).

Figure 1: Cell assembly of the vapor electrolyzer MEA

Figure 2: a) The nondimensionalized limiting current density is shown as a function of β, the net water flux in the membrane normalized by the proton flux b) The current density for β=0 as a function of temperature assuming 98% RH in the gas channel.

Figure 3: Electrolysis at (a) 30°C, blue and (b) 80°C, red for both liquid-fed (circles) and vapor-fed (squares) cells. Operating conditions: Nafion 117 membrane; 1 mg/cm$^2$ iridium loading on anode, and 0.3 mg /cm$^2$ Pt from Pt/C on cathode, and vapor feed at 98% RH on both sides flowing at 200 mL/min.

Figure 4: a) Model fit of the vapor-fed MEA operating at 98% RH system at 80°C with the HFR data corresponding to the experiments (circles, right axis) and b) applied voltage breakdown for this system c) RH (green) and water content (purple), defined as moles of water per mole sulfonic acid site, throughout the cell at 150 mA/cm$^2$ (dashed) and 680 mA/cm$^2$ (bold).

Figure 5: (a) Difference in cell potential when the carrier gas is changed from helium (2 g/mol) to argon (MW = 40 g/mol), so a negative change is potential is a lower overpotential. The square points show experimental measurements and the solid line shows the predictions of the model (left axis). The difference in membrane water content, λ, is shown on the right axis for Nafion 117, where the increasing trend shows a higher λ in helium with increasing current density. (b) Electrolyzer performance for Nafion 117 (183 μm) vs. Nafion 211 (25 μm). Experiments were carried out at 80 °C with an iridium loading 1 mg/cm$^2$ on the anode and a Pt from Pt/C loading of 0.3 mg /cm$^2$ on the cathode. The anode and cathode feed flow rate were 200 mL/min and the RH was 98% for both feeds.

Figure 6: Polarization curves at various RH for vapor electrolysis from 98% RH (dark blue), 50% RH (blue), and 30% RH (light blue). Points are experimental data; solid lines are from the model. Vapor electrolyzer experiments and model were ran and simulated at 80 °C, with Nafion 117 membrane; the anode had 1 mg/cm$^2$ iridium loading, the cathode had 0.3 mg Pt/cm$^2$ using Pt/C loading.

Figure 7: a) AVBs at a constant current density of 150 mA/cm$^2$ shown as a function of humidity. b) Percent contribution to the total cell voltage, simulated at 80 °C. AVBs for 30% and 50% RH are given in Figure S7a and b.

Figure 8:a) Reaction distributions, b) water content and c) overpotential for varying RH conditions within the nondimensionalized anode catalyst layer at 150 mA/cm$^2$.

Figure 9: a) Polarization curves for asymmetric study (triangles and circles) and the average cell RH humidity symmetric study (squares) for comparison. The cathode (circles) and anode (triangles) had the inlet RH of 30% while the other electrode was kept at 98% b) Values of β as a function of current density for each of the three cases calculated using the model of a vapor-fed electrolyzer.

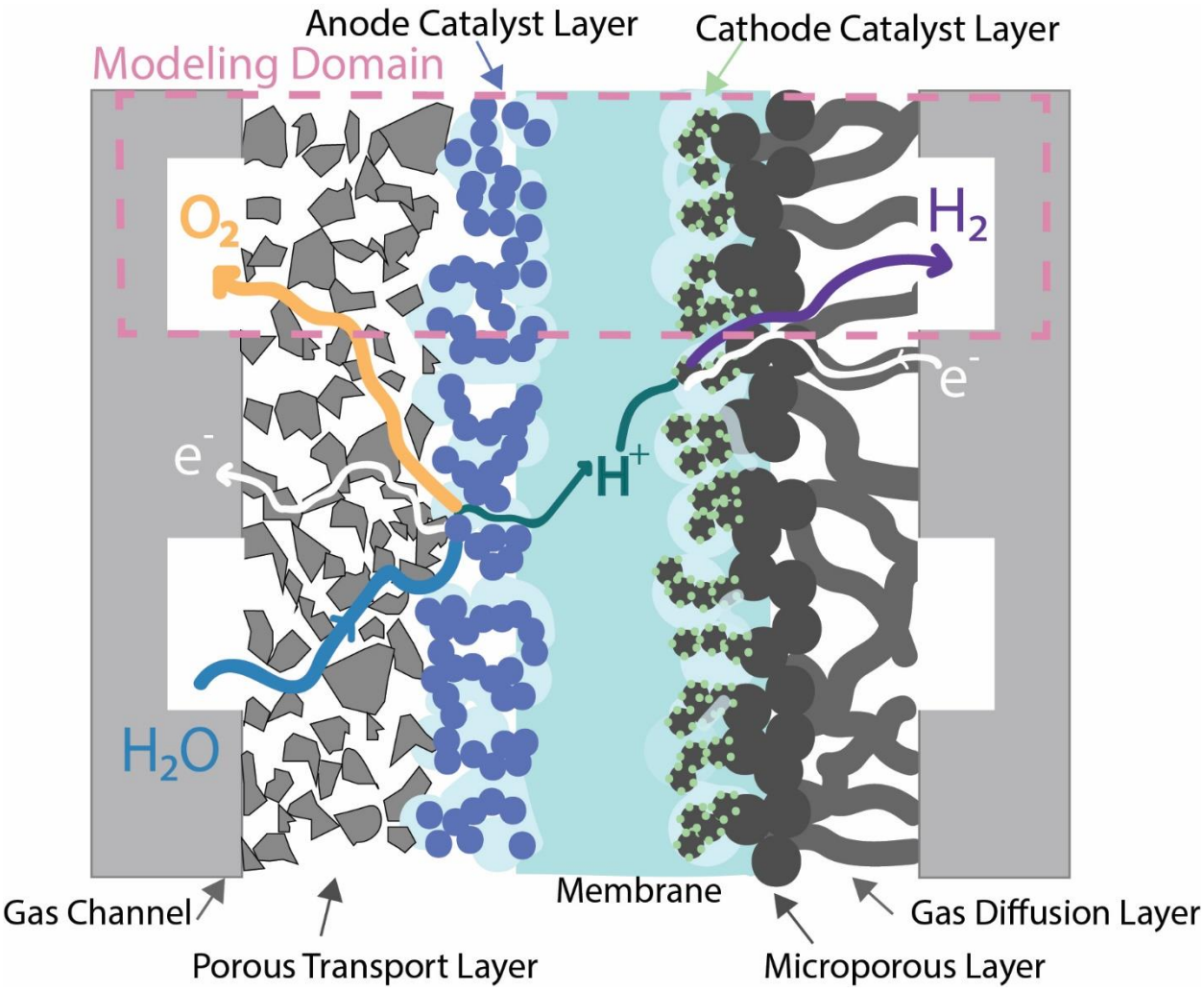
Anode Catalyst Layer
Cathode Catalyst Layer
Modeling Domain
O2
H2
e-
e-
H+
H2O
Gas Channel
Porous Transport Layer
Membrane
Microporous Layer
Gas Diffusion Layer

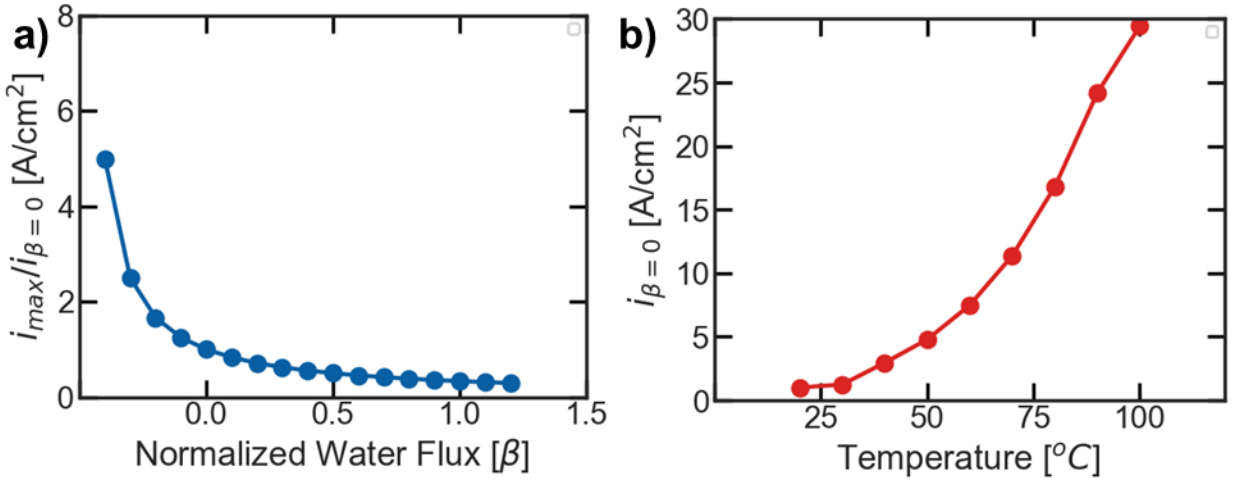
a)
$i_{max}/i_{\beta=0}$ [A/cm$^2$]
Normalized Water Flux [$\beta$]
b)
$i_{\beta=0}$ [A/cm$^2$]
Temperature [$^oC$]

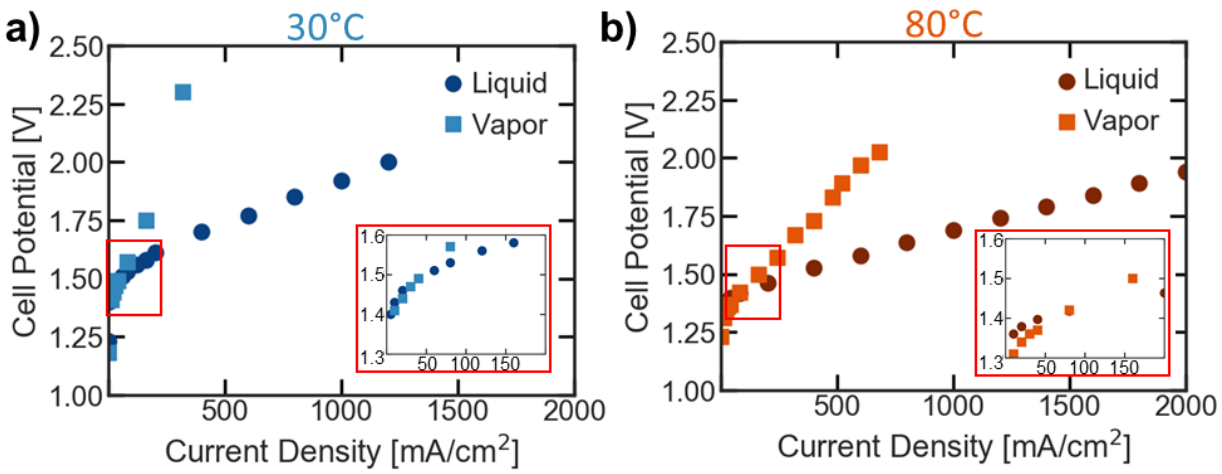
a)
30°C
Liquid
Vapor
Cell Potential [V]
Current Density [mA/cm$^2$]
b)
80°C
Liquid
Vapor
Cell Potential [V]
Current Density [mA/cm$^2$]

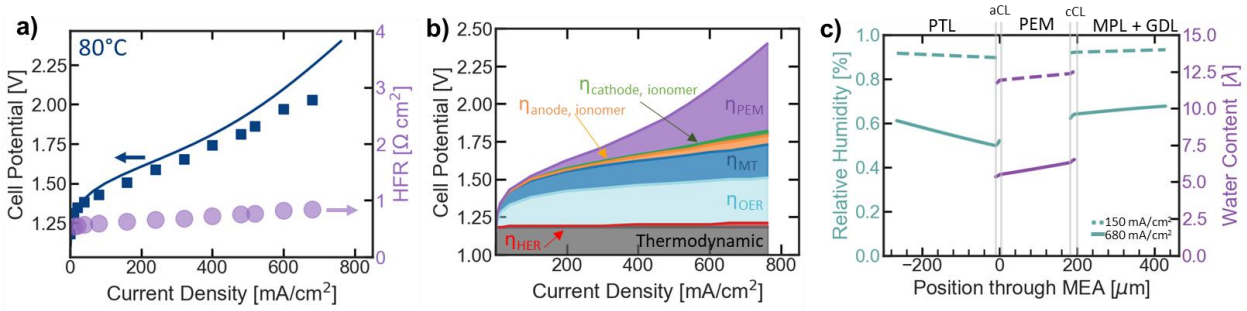
a)
80°C
Cell Potential [V]
HFR [Ω cm²]
Current Density [mA/cm²]
b)
Cell Potential [V]
η cathode, ionomer
η anode, ionomer
η PEM
η MT
η OER
η HER
Thermodynamic
Current Density [mA/cm²]
c)
PTL
aCL
PEM
cCL
MPL + GDL
Relative Humidity [%]
Water Content [λ]
150 mA/cm²
680 mA/cm²
Position through MEA [μm]

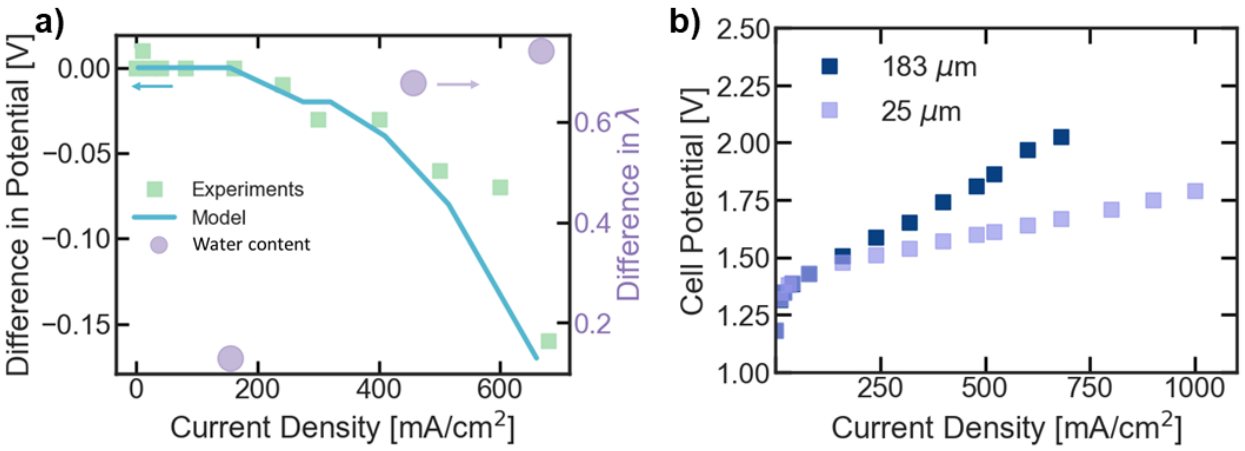
a)
Difference in Potential [V]
0.00
−0.05
−0.10
−0.15
0
200
400
600
Current Density [mA/cm$^2$]
Experiments
Model
Water content
0.6
0.4
0.2
Difference in λ
b)
Cell Potential [V]
2.50
2.25
2.00
1.75
1.50
1.25
1.00
250
500
750
1000
Current Density [mA/cm$^2$]
183 μm
25 μm

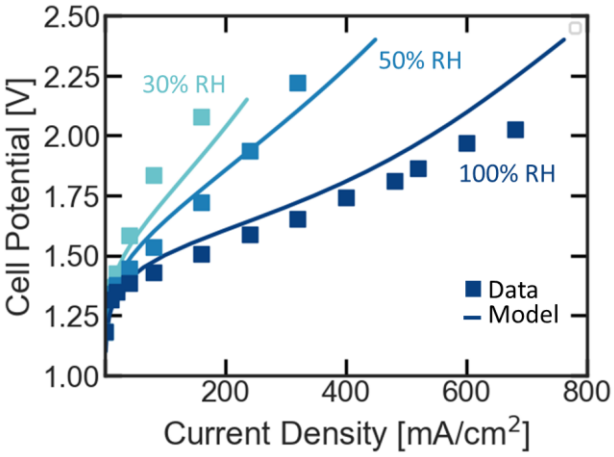
2.50
2.25
2.00
1.75
1.50
1.25
1.00
Cell Potential [V]
30% RH
50% RH
100% RH
Data
Model
200
400
600
800
Current Density [mA/cm2]

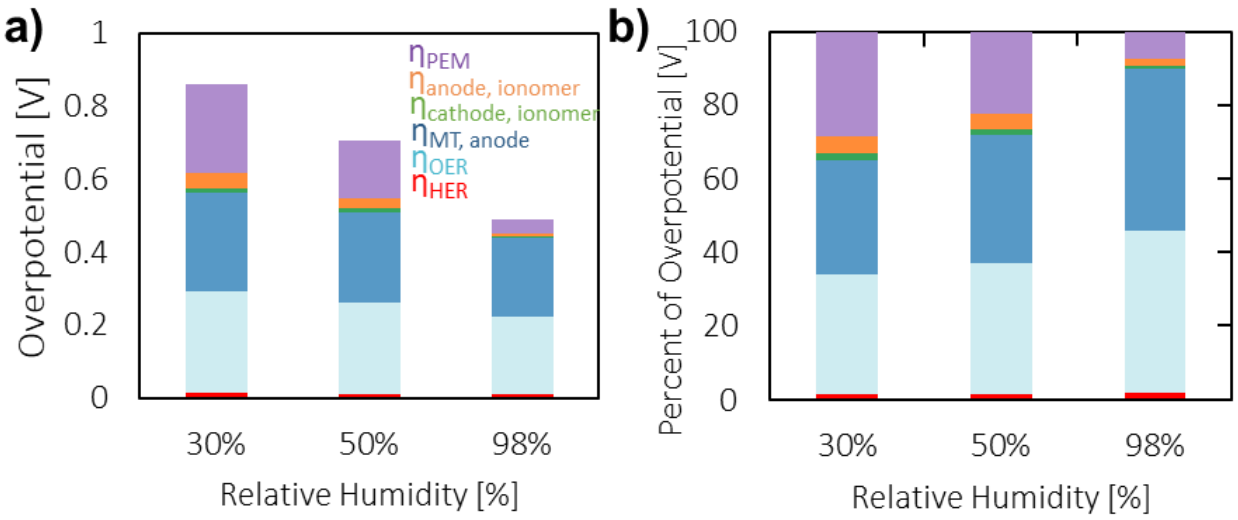
a)
Overpotential [V]
1
0.8
0.6
0.4
0.2
0
ηPEM
ηanode, ionomer
ηcathode, ionomer
ηMT, anode
ηOER
ηHER
30%
50%
98%
Relative Humidity [%]
b)
Percent of Overpotential [V]
100
80
60
40
20
0
30%
50%
98%
Relative Humidity [%]

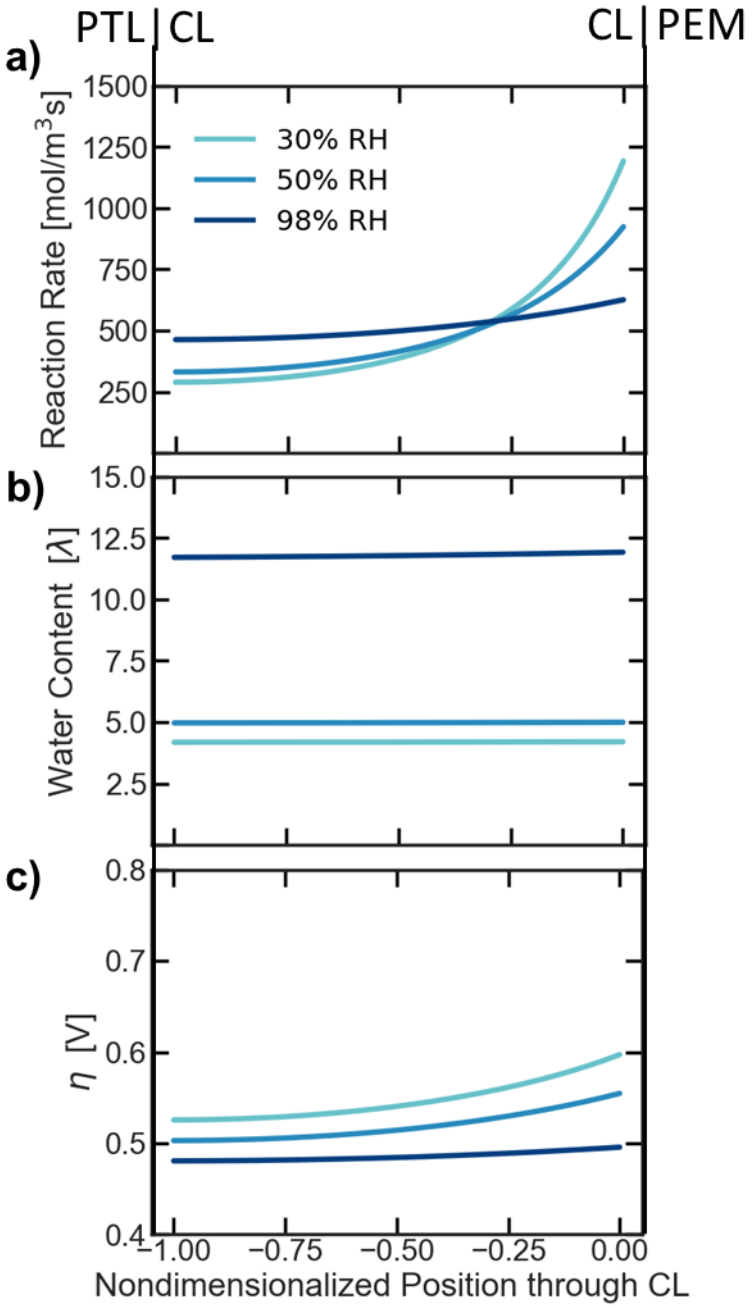
PTL
CL
CL
PEM
a)
Reaction Rate [mol/m$^3$s]
1500
1250
1000
750
500
250
30% RH
50% RH
98% RH
b)
Water Content [λ]
15.0
12.5
10.0
7.5
5.0
2.5
c)
η [V]
0.8
0.7
0.6
0.5
0.4
−1.00
−0.75
−0.50
−0.25
0.00
Nondimensionalized Position through CL

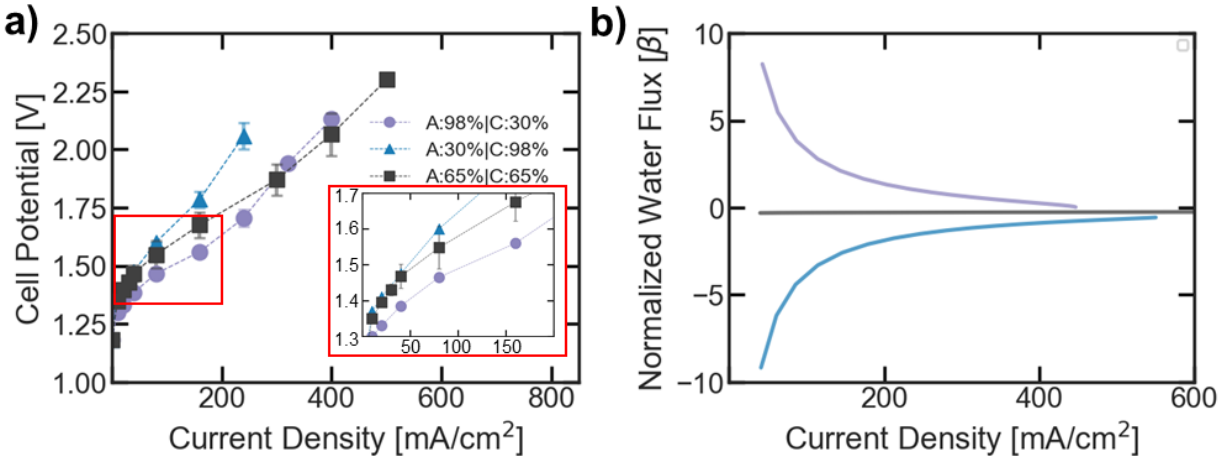
a)
Cell Potential [V]
Current Density [mA/cm$^2$]
A:98%|C:30%
A:30%|C:98%
A:65%|C:65%
b)
Normalized Water Flux [$\beta$]
Current Density [mA/cm$^2$]